Low lattice thermal conductivity and good thermoelectric performance of cinnabar

Yinchang Zhao,[1,*] Zhenhong Dai,[1,†] Chao Lian,[2] Shuming Zeng,[3] Geng Li,[3] Jun Ni,[3,4,‡] and Sheng Meng[2,4,§]

[1]*Department of Physics, Yantai University, Yantai 264005, People's Republic of China*

[2]*Beijing National Laboratory for Condensed Matter Physics and Institute of Physics, Chinese Academy of Sciences, Beijing, 100190, People's Republic of China*

[3]*State Key Laboratory of Low-Dimensional Quantum Physics, Department of Physics, Tsinghua University, Beijing 100084, People's Republic of China*

[4]*Collaborative Innovation Center of Quantum Matter, Beijing 100084, People's Republic of China*

(Received 16 July 2017; published 7 November 2017)

Based on the combination of first-principles calculations, Boltzmann transport equation, and electron-phonon interaction (EPI), we investigate the thermal and electronic transport properties of crystalline cinnabar (α-HgS). The calculated lattice thermal conductivity κ_L is remarkably low, e.g., 0.60 $\mathrm{Wm^{-1}\,K^{-1}}$ at 300 K, which is about 30% of the value for the typical thermoelectric material PbTe. Via taking fully into account the **k** dependence of the electron relaxation time computed from the EPI matrix, the accurate numerical results of thermopower S, electrical conductivity σ, and electronic thermal conductivity κ_E are obtained. The calculated power factor $S^2\sigma$ is relatively high while the value of κ_E is negligible, which, together with the fairly low κ_L, leads to a good thermoelectric performance in the n-type doped α-HgS, with the figure of merit zT even exceeding 1.4. Our analyses reveal that (i) the large weighted phase space and the quite low phonon group velocity result in the low κ_L, (ii) the presence of flat band around the Fermi level combined with the large band gap causes the high S, and (iii) the small electron linewidths of the conduction band lead to a large relaxation time and thus a relatively high σ. These results support that α-HgS is a potential candidate for thermoelectric applications.

DOI: 10.1103/PhysRevMaterials.1.065401

I. INTRODUCTION

The focus on thermoelectric (TE) materials has increased drastically because of their power for converting heat into electricity. For a TE power generator, the conversion efficiency is determined by the dimensionless figure of merit $zT = S^2\sigma T/(\kappa_L + \kappa_E)$, where S is the thermopower (Seebeck coefficient), σ the electrical conductivity, T the absolute temperature, and κ_L (κ_E) the lattice (electronic) thermal conductivity. Due to the Wiedemann-Franz formula $\kappa_E = L\sigma T$ (L is the Lorenz number), optimization of the figure of merit zT is subject to the interdependence between σ and κ_E, which means that to tune κ_E independently is almost impossible. Hence, to improve zT, researchers have been turning to seek out schemes to reduce the lattice thermal conductivity κ_L or to enhance the TE power factor $S^2\sigma$ [1–8]. For instance, a high zT of 2.2 was reported in the bulk spark-plasma-sintered Na-doped PbTe:SrTe at 900 K, due to the significant reduction of κ_L to 0.5 $\mathrm{Wm^{-1}\,K^{-1}}$ by the all-scale hierarchical structures [1]. A $zT \sim 2.0$ was obtained in the Na-doped PbTe at 773 K through optimization of the nanostructures to reduce the κ_L [2]. A zT of 1.5 was achieved at 773 K in the Tl-doped p-type PbTe, because of a sharp enhancement of S resulted from the distortion of the electronic density of states (EDOS) [3,4]. The zT of the low-dimensional Bi_2Te_3 is increased by a factor of 13 over the bulk value via the quantum confinement effect, since S and σ can be tuned by the highly anisotropic effective-mass tensor [5]. In addition, there are numerous materials with low κ_L and good TE properties, such as $IrSb_3$ [9], CdO [10], $PbTiO_3$ [11], fully filled skutterudite $YbFe_4Sb_{12}$ [12], n-type TiO_2 polymorphs [13], and nanoporous bulk silicon [14], etc. From the viewpoint of composition, most of these materials contain heavy elements, which is beneficial for decreasing the phonon velocity and phonon lifetimes and thus helps reducing the κ_L. Ideally, the material possessing low κ_L and high $S^2\sigma$ simultaneously will be the best candidate for TE applications. Enlightened by the composition of heavy elements and the semiconducting character, here we turn to the ancient material cinnabar to search the low κ_L and good TE performance.

Cinnabar, the main ingredient constituting red pigment termed vermillion which was already used in ancient times, is the most common source ore for the production of elemental mercury. The single crystal of cinnabar (α-HgS) is crystallized in the trigonal structure, which can be pried out of the mineral samples or grown from the elements through conventional vapor phase techniques [15]. The trigonal α-HgS is the stable form of mercuric sulfide under normal temperature and pressure. Meanwhile, its polymorph, metacinnabar (β-HgS, a zincblendelike configuration), is also found in nature, and can be grown experimentally through adding traces of iron ($\sim$1%) to the elements utilized in the growth. For pure α-HgS samples, the phase transition to β-HgS occurs at about 673 K and becomes complete at 698 K due to the kinetics reasons [16]. While β-HgS is a zero-gap semimetal, α-HgS is an anisotropic semiconductor with a large band gap and highly dichroic character of the absorption coefficient, which thus makes it be an interesting material. To date the electronic [17–20], vibrational [20–23], optical [24–26], luminescence [26,27], photoelectronic [28,29], and photoemission [30] properties of α-HgS have been investigated to an extensive extent. However, the thermal transport and TE properties of α-HgS are not yet known, although the characters of thermal expansion and

*y.zhao@ytu.edu.cn
†zhdai@ytu.edu.cn
‡junni@mail.tsinghua.edu.cn
§smeng@iphy.ac.cn

 ©2017 American Physical Society

specific heat were once reported [16,20]. In this paper, we systematically investigate the thermal and electronic transport properties of α-HgS and conclude that this material possesses low lattice thermal conductivity κ_L and high power factor $S^2\sigma$. As a result, a figure of merit zT even exceeding 1.4 is achieved in the n-type doped α-HgS. These results indicate that α-HgS is a potential candidate for future TE applications.

II. METHODOLOGY

The lattice thermal transport properties are calculated by the phonon Boltzmann transport equation (BTE) together with the interatomic force constants (IFCs) obtained from first-principles techniques. From the solution of phonon BTE [31], the lattice thermal conductivity along the α axis is written as

$$\kappa_L^{\alpha\alpha} = \frac{1}{k_B T^2 N_q \Omega} \sum_{\mathbf{q}\nu} n_{\mathbf{q}\nu}(n_{\mathbf{q}\nu}+1)(\hbar\omega_{\mathbf{q}\nu})^2 v_{\mathbf{q}\nu}^{\alpha} F_{\mathbf{q}\nu}^{\alpha}, \quad (1)$$

where k_B, N_q, and Ω are Boltzmann constant, the number of q points in the Brillouin zone (BZ), and the volume of the unit cell, respectively. $n_{\mathbf{q}\nu}$ is the equilibrium Bose-Einstein distribution function of phonon mode $\mathbf{q}\nu$. $v_{\mathbf{q}\nu}^{\alpha}$ is the phonon group velocity along the α axis. $F_{\mathbf{q}\nu}^{\alpha}$ is given by $F_{\mathbf{q}\nu}^{\alpha} = \tau_{\mathbf{q}\nu}^{ph}(v_{\mathbf{q}\nu}^{\alpha} + \Delta_{\mathbf{q}\nu})$, where $\tau_{\mathbf{q}\nu}^{ph}$ is the phonon lifetime of mode $\mathbf{q}\nu$ in relaxation time approximation (RTA), $\Delta_{\mathbf{q}\nu}$ is a term used to correct the inaccuracy of RTA via solving the BTE iteratively. If $\Delta_{\mathbf{q}\nu} = 0$, the RTA result of $\kappa_L^{\alpha\alpha}$ is obtained.

The ShengBTE code [31] is applied to calculate the κ_L. The harmonic and anharmonic IFCs are computed based on the density functional theory (DFT) by the combination of the VASP package [32,33], PHONOPY program [34], and THIRDORDER.PY script [31]. They are both generated within $4 \times 4 \times 2$ supercells by the finite-difference approach, and the interaction up to fifth-nearest neighbors is included in the calculations of anharmonic IFCs. The ion cores are modeled by the projector augmented wave potentials (PAW) [35], and the valance electrons are described by a plane-wave basis set with the cutoff energy of 400 eV and the exchange-correlation functional of generalized gradient approximation (GGA) of Perdew-Burke-Ernzerhof (PBE) [36]. For comparison, the local density approximation (LDA) exchange-correlation functional is also used to calculate the structural, electronic, and vibrational properties. For the primitive cell, the force of 10^{-6} eV/Å acting on each atom and the electronic convergence criterion of 10^{-8} eV are selected to relax the structure, and a $12 \times 12 \times 6$ Γ-centered Monkhorst-Pack electron-momentum grid is used to simulate the BZ integration. For the calculations of supercells, due to the small BZ induced by the enlarged lattice parameters, only the Γ point is chosen in the BZ summation, and the rationality of this choice is confirmed by the subsequent phonon dispersion calculations. For ShengBTE calculations, a phonon wave-vector mesh of $24 \times 24 \times 12$ is used to simulate the corresponding $\mathbf{q}$ space integration.

For calculations of the electronic transport properties, the electron Boltzmann theory and the rigid band approach are applied with the $\mathbf{k}$ dependent electron relaxation time, which is computed from the electron-phonon interaction (EPI), as the input quantity. From the electron Boltzmann theory [37], we can obtain thermopower S, electrical conductivity σ, and electronic thermal conductivity κ_E along the α axis as follows

$$S_{\alpha\alpha} = -\frac{1}{eT} \frac{\sum_{n\mathbf{k}}(\varepsilon_{n\mathbf{k}} - \varepsilon_F)\left(v_{n\mathbf{k}}^{\alpha}\right)^2 \tau_{n\mathbf{k}}^{el} \frac{\partial f_{n\mathbf{k}}}{\partial \varepsilon_{n\mathbf{k}}}}{\sum_{n\mathbf{k}} \left(v_{n\mathbf{k}}^{\alpha}\right)^2 \tau_{n\mathbf{k}}^{el} \frac{\partial f_{n\mathbf{k}}}{\partial \varepsilon_{n\mathbf{k}}}}, \quad (2)$$

$$\sigma_{\alpha\alpha} = -\frac{e^2}{N_k \Omega} \sum_{n\mathbf{k}} \left(v_{n\mathbf{k}}^{\alpha}\right)^2 \tau_{n\mathbf{k}}^{el} \frac{\partial f_{n\mathbf{k}}}{\partial \varepsilon_{n\mathbf{k}}}, \quad (3)$$

$$\kappa_E^{\alpha\alpha} = -\frac{1}{N_k \Omega T} \sum_{n\mathbf{k}} (\varepsilon_{n\mathbf{k}} - \varepsilon_F)^2 \left(v_{n\mathbf{k}}^{\alpha}\right)^2 \tau_{n\mathbf{k}}^{el} \frac{\partial f_{n\mathbf{k}}}{\partial \varepsilon_{n\mathbf{k}}} - T S_{\alpha\alpha}^2 \sigma_{\alpha\alpha}, \quad (4)$$

where ε_F, $\varepsilon_{n\mathbf{k}}$, and N_k are Fermi energy, energy eigenvalue of the Khon-Sham state $n\mathbf{k}$, and the total number of k points in the full BZ, respectively. $f_{n\mathbf{k}}$ is the Fermi-Dirac distribution function, and $v_{n\mathbf{k}}^{\alpha}$ is the electron group velocity along the α axis. $\tau_{n\mathbf{k}}^{el}$ is the electron relaxation time, which is calculated according to the relationship

$$\tau_{n\mathbf{k}}^{el} = \frac{\hbar}{2\Sigma_{n\mathbf{k}}''}, \quad (5)$$

where $\Sigma_{n\mathbf{k}}''$ is the imaginary part of electron self-energy, also known as electron linewidth. $\Sigma_{n\mathbf{k}}''$ can be obtained from the EPI by the formula [38]

$$\Sigma_{n\mathbf{k}}'' = \frac{\pi}{\hbar} \sum_{m\nu} \int_{BZ} \frac{d\mathbf{q}}{\Omega_{BZ}} |g_{mn,\nu}(\mathbf{k},\mathbf{q})|^2 \times \{(n_{\mathbf{q}\nu} + f_{m\mathbf{k}+\mathbf{q}})\delta[\hbar\omega - (\varepsilon_{m\mathbf{k}+\mathbf{q}} - \varepsilon_F) + \hbar\omega_{\mathbf{q}\nu}] + (n_{\mathbf{q}\nu} + 1 - f_{m\mathbf{k}+\mathbf{q}})\delta[\hbar\omega - (\varepsilon_{m\mathbf{k}+\mathbf{q}} - \varepsilon_F) - \hbar\omega_{\mathbf{q}\nu}]\}, \quad (6)$$

where $g_{mn,\nu}(\mathbf{k},\mathbf{q})$ is the EPI matrix element induced by phonon mode $\mathbf{q}\nu$ between the states m$\mathbf{k}$+$\mathbf{q}$ and n$\mathbf{k}$.

The EPI is calculated by the density functional perturbation theory (DFPT) and Wannier interpolation technique [39]. The calculations are initially carried out within the $8 \times 8 \times 4$ electron-momentum grid and the $4 \times 4 \times 2$ phonon wave-vector mesh by the QUANTUM-ESPRESSO package [40]. Then the results are interpolated into a dense mesh of $40 \times 40 \times 20$ for both of the electron momentum and phonon wave vector by using the maximally localized Wannier functions as coded in the EPW package [38,41]. In these calculations, the norm-conserving pseudopotential, the GGA-PBE exchange-correlation functional, and the energy cutoff of 120 Ry are used. The structural, electronic, and vibrational properties are recalculated by QUANTUM-ESPRESSO and EPW, and consistent results with those calculated by VASP and PHONOPY are obtained.

III. RESULTS AND DISCUSSION

α-HgS has two chiral (enantiomorphic) configurations with the symmetric groups of $P3_121$ and $P3_221$, as shown in Fig. 1(a). Its primitive cell is composed of two coaxial helices with one formed by three Hg atoms and the other by three S atoms. The optimized lattice parameters are $a \sim 4.389$ Å, $c \sim 9.707$ Å ($a \sim 4.023$ Å, $c \sim 9.286$ Å) from the GGA (LDA) calculations, which are higher (lower) than the experimental

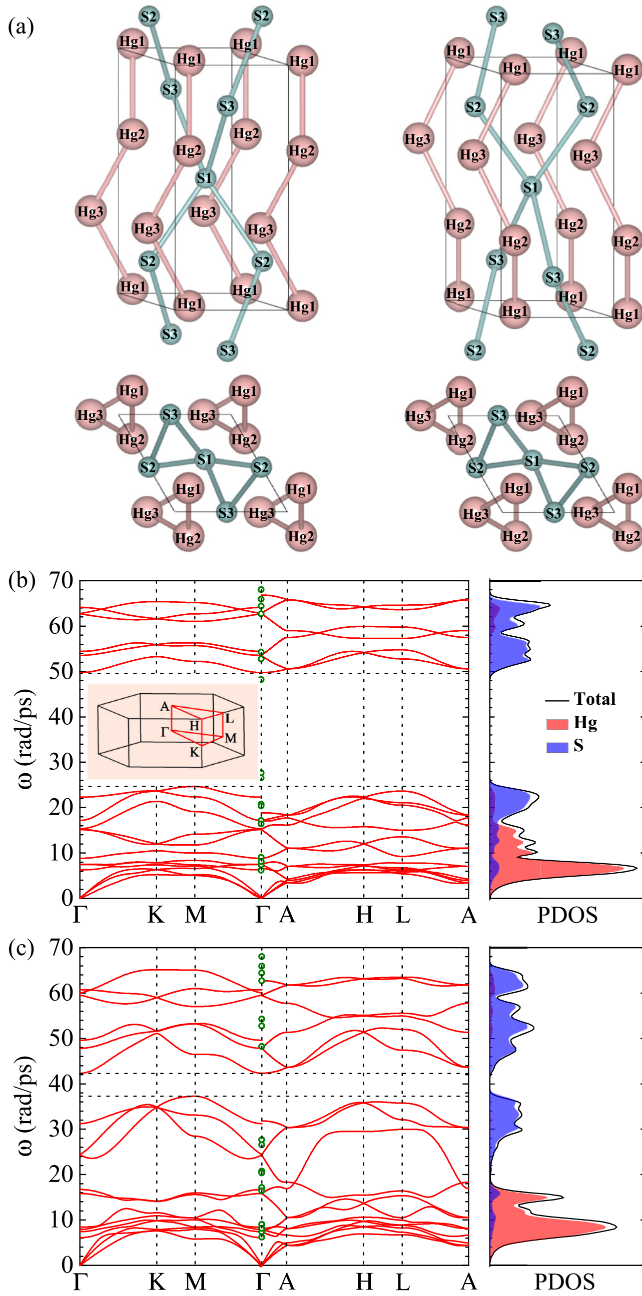

FIG. 1. (a) Lateral and top view of α-HgS with the symmetric groups of $P3_121$ (left) and $P3_221$ (right). (b) Phonon dispersion and PDOS of α-HgS calculated with GGA. (c) Same as (b) but calculated with LDA. In (b) and (c), the green circles denote the Raman and ir-active phonons around the Γ point (Ref. [21]). The inset in (b) shows the whole Brillouin zone (BZ) of α-HgS with the irreducible BZ designated by the red framework.

values of $a \sim 4.15$ Å, $c \sim 9.50$ Å [42], and consistent with previous calculations with the same exchange-correlation functional [20].

The phonon dispersion and phonon density of states (PDOS) calculated with GGA and LDA are plotted in Figs. 1(b) and 1(c), respectively. Because of the lacking of experimental results for the phonon dispersion in the whole BZ, only the experimental data for Raman and ir spectroscopy are shown for comparison [21]. In our calculations, nonanalytical term correction is considered to include the effect of polarization field on optical phonon behavior around the Γ point. Due to the strong anisotropy of the polarization, there exists a different correction along the nonequivalent direction, which, as a result, leads to a small discontinuity of phonon dispersion at the Γ point when the phonon wave vector changes direction from the MΓ or KΓ line to the ΓA line. Although the inclusion of the nonanalytical term correction is not very accurate to describe the optical phonons at the Γ, our results show excellent agreement with previous work calculated with the same exchange-correlation functional, as shown in Fig. 9 of Ref. [20], which indicates the basic reliability of our calculations. The partial PDOS indicates that the low-frequency phonons are mainly afforded by Hg atoms while most of the high-frequency modes originate from the vibrations of S atoms, which is resulted from the heavier mass of Hg than that of S. The existence of six atoms in each primitive cell give rise to 18 phonon branches (three acoustic and 15 optical branches). The optical modes are divided into nine low-frequency branches and six high-frequency branches by a gap near to the frequency of 40 rad/ps. Strikingly, the GGA calculations give a large value of 24.7 rad/ps for the gap, while the LDA results show the gap value of only 5.1 rad/ps. At the Γ point, the GGA results overestimate the gap by about 29% compared with the Raman and ir spectroscopy, in contrast to that the LDA calculations underestimate the gap by 51%. Overall, the GGA results are much more consistent with the experimental data for Raman and ir spectroscopy, especially for the six high-frequency optical branches, as shown in Fig. 1(b). Hence, the exchange-correlation functional of GGA is selected to calculate the subsequent thermal transport properties.

The calculated κ_L of the naturally occurring α-HgS as a function of T is plotted in Fig. 2. Since the phase transition from α-HgS to β-HgS occurs at about 673 K and becomes complete at 698 K [16], we show the values of κ_L below 700 K in Fig. 2. The iterative solutions (ITS) of the BTE and the RTA results are both shown, which indicates a difference of about 12% (3%) for the κ_L along the a (c) axis. For comparison, the ITS result for the κ_L of the typical TE material PbTe is also shown in Fig. 2, which is computed by the same methods and precisions as the calculations of α-HgS, and the result is well consistent with the previous work [43]. Remarkably, for α-HgS the values of the κ_L along a and c axes are both fairly low. For instance, the ITS (RTA) results of the κ_L along the a axis is only 0.60 (0.52) $\mathrm{Wm^{-1}K^{-1}}$ at 300 K, which is about 30% of the value for PbTe, and nearly comparable with the κ_L of the full Heusler semiconductors Ba_2HgPb and Ba_2HgSn [44]. The κ_L along the c axis is about 60% to 80% higher than that along the a axis as the temperature changing from 100 to 700 K, which implies a strong anisotropy of the thermal transport performance of α-HgS. In addition, the isotope effect is also studied, which has a tiny influence (<3%) on the determination of κ_L at $T \geqslant 300$ K, see S1 in Ref. [45].

Furthermore, we also investigate the cumulative thermal conductivity κ_C versus the allowed phonon frequency and phonon maximum mean-free path (MFP), respectively, as shown by the insets in Fig. 2. The κ_C versus the phonon frequency gives the summed contribution from all phonon

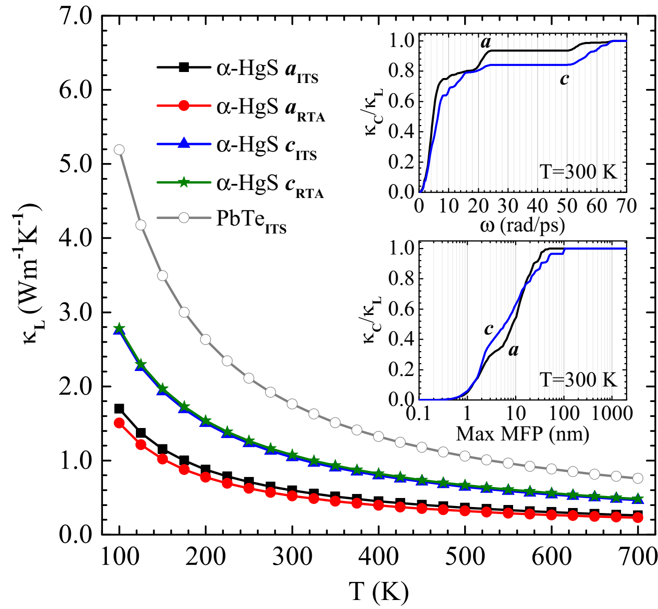

FIG. 2. Lattice thermal conductivity κ_L *vs* temperature T for naturally occurring α-HgS calculated with GGA. The square (solid circle) and triangle (pentagram) lines represent the ITS (RTA) results along a and c axes, respectively. The hollow circle line is the ITS result for the κ_L of PbTe for comparison. The insets show the cumulative thermal conductivity κ_C (re-scaled by κ_L) *vs* the phonon frequency (top) and the phonon maximum mean-free path (MFP) (bottom) at 300 K.

modes below the specified frequency, which indicates that about 76% (68%) of the total κ_L along the a (c) axis is dominated by the phonon modes with the frequency below 10 rad/ps, meaning that the low-frequency phonons are responsible for the thermal transport of α-HgS. The κ_C versus the phonon maximum MFP reveals the size dependence of the κ_L, which exhibits that the phonons with a MFP smaller than about 18 nm dominate about 80% of the total κ_L along both a and c axes, implying that the nanostructures with a characteristic length of the phonon MFP shorter than 18 nm are required to reduce the κ_L significantly.

To reveal the hidden physical mechanism of the low κ_L of α-HgS, we show the anharmonic three-phonon scattering rates (ASRs) versus phonon frequency in Fig. 3(a). In the RTA, the total scattering rates $1/\tau^{\mathrm{ph}}_{\mathbf{q}\nu}$ of mode $\mathbf{q}\nu$ is obtained from the ASRs $1/\tau^{\mathrm{anh}}_{\mathbf{q}\nu}$ and the isotopic scattering rates (ISRs) $1/\tau^{\mathrm{iso}}_{\mathbf{q}\nu}$ by the relation of $1/\tau^{\mathrm{ph}}_{\mathbf{q}\nu} = 1/\tau^{\mathrm{anh}}_{\mathbf{q}\nu} + 1/\tau^{\mathrm{iso}}_{\mathbf{q}\nu}$. The ISRs are much lower than the ASRs (see S2 in Ref. [45]), interpreting the negligible influence of isotopic mass variance on the determination of κ_L. Thus, the ASRs are responsible for the total scattering rates of α-HgS. As shown in Fig. 3(a), the ASRs of α-HgS at 300 K are overall slightly lower than those of PbTe at the same temperature. However, for the phonon modes with the frequency below about 5 rad/ps, which play a significant role in thermal transport of both α-HgS and PbTe, the ASRs of α-HgS are nearly comparable with those of PbTe. In addition, the process dependent ASRs show that for α-HgS the ASRs of the modes below about 8 rad/ps are mainly resulted from the phonon absorption processes (ASRs^+), as shown in Fig. 3(a).

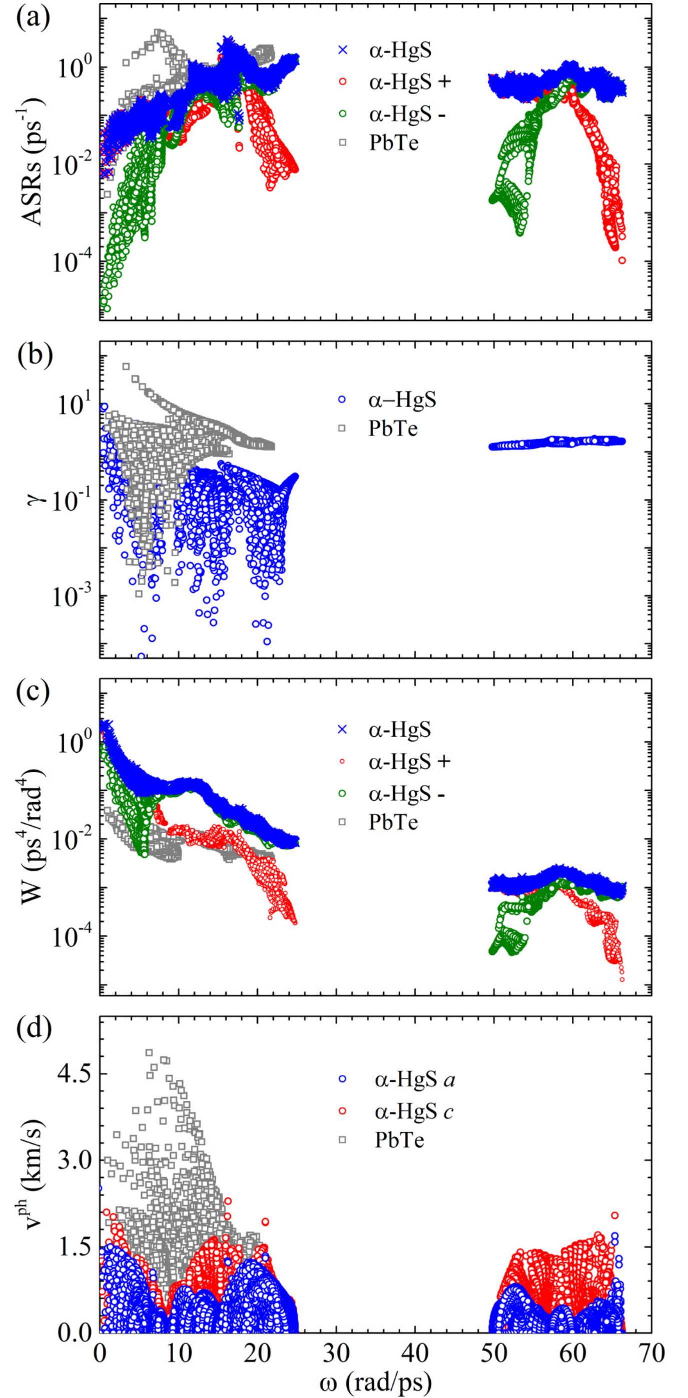

FIG. 3. Anharmonic three-phonon scattering rates (ASRs) (a), Gruneisen parameter γ (b), weighted phase space W (c), and phonon group velocity v^{ph} (d) as functions of phonon frequency for α-HgS. The results for ASRs and W of phonon absorption (+) and emission (−) processes are also shown in (a) and (c). The corresponding values of PbTe are shown for comparison.

As is known, the ASRs derive from the sum of three-phonon transition probabilities, which are determined by the anharmonic IFCs and the weighted phase space W. The strength of the anharmonic IFCs corresponds to the anharmonicity of a phonon mode, which is usually characterized by the Gruneisen parameter γ. The weighted phase space W is a direct measure

of the number of scattering processes [12,46]. Our results show that the mode dependent Gruneisen parameters γ of α-HgS are much smaller than the values of PbTe, as shown in Fig. 3(b). As a result, the total γ of only 0.60 is obtained in α-HgS, which is much lower than the value of 2.12 in PbTe, and thus indicates a weak anharmonicity in α-HgS. Nevertheless, the weighted phase spaces W of α-HgS are fairly high compared with those of PbTe, as shown in Fig. 3(c), which compensate the weak anharmonicity and consequently give rise to the ASRs nearly as strong as those of PbTe. Moreover, for the phonon modes below 8 rad/ps, the total W is also dominated by the phonon absorption processes (W^+), interpreting that the total ASRs are governed mainly by the ASRs$^+$ at this frequency range.

Another significant factor determining the thermal transport performance is the phonon group velocity v^{ph}. As shown in Fig. 3(d), for α-HgS the phonon group velocities along a and c axes are both much lower than those of PbTe. In view of $\kappa_L \propto v^2_{\mathbf{q}\nu}$ in the RTA, the presence of these fairly low group velocities is the primary factor that makes the κ_L of α-HgS be much lower than the κ_L of PbTe. In addition, due to the helix features along the c axis of α-HgS, there exist the slant linear $\mathbf{q}$ terms in the phonon dispersion along the ΓA line [20], as shown in Fig. 1(b), which, as a result, gives rise to a relatively high phonon group velocity along the c axis, as shown in Fig. 3(d), and thus interprets the higher κ_L along this axis. Furthermore, based on the group velocities and the ASRs, we can also analyze the polarization dependent κ_L of α-HgS. We find that three acoustic phonon branches contribute about 66% (43%) of the total κ_L along the a (c) axis. Noticeably, due to the linear dispersion of the softest optical phonon branch along ΓA line, as shown in Fig. 1(b), about 12% of the total κ_L along the c axis is provided by the softest optical phonon modes (see S3 in Ref. [45]).

The low κ_L of α-HgS would make it be a promising TE candidate if its thermopower S and electrical conductivity σ are high enough. Since the electronic transport properties depend on the electronic structures, we study the band structure and electronic density of states (EDOS) of α-HgS firstly. The exchange-correlation functionals of GGA and LDA are both used to calculate these properties. The band structure and EDOS calculated with GGA are shown in Fig. 4(a). It is found that α-HgS has an indirect band gap of about 1.67 eV, with the conduction band minimum (CBM) at the Γ point and the valence band maximum (VBM) around the center point of the ΓA line. Meanwhile, the direct band gap at the Γ point is about 1.70 eV. These band gaps are smaller about 25% than the experimentally reported value $\sim$2.25 eV [47], but accord with the previous results calculated with the same exchange-correlation functional [19]. Partial EDOS shows that the valence band is mainly contributed by the S $3p$ orbitals, while the conduction band arises from the hybridization state of Hg $6s$, Hg $5d$, and S $3p$ electrons. In addition, the band structure calculated with LDA show a band gap of only 0.83 eV (see S4 in Ref. [45]), which is well consistent with the previous work with the LDA gap of 0.82 eV [20]. Considering that the GGA band gap is more close to the experimental value, the exchange-correlation functional of GGA is used to calculate the subsequent electronic transport properties.

Prominently, the band gap of 1.67 eV for α-HgS is much higher than the values for most of the known TE materials.

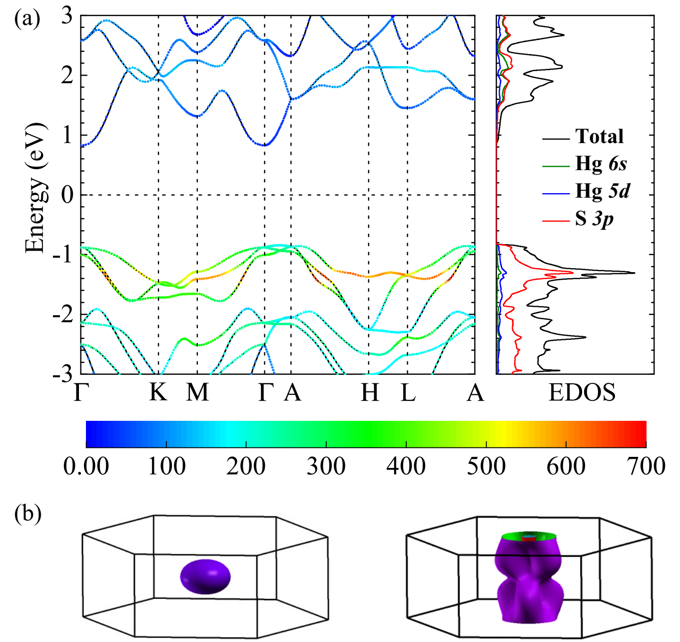

FIG. 4. (a) The band structure with projections of electron linewidths (left) and the EDOS (right) for α-HgS calculated with GGA. The size of the projections of electron linewidths are scaled by the bottom color bar with the unit of meV. (b) The isoenergy surface of α-HgS for E_F dipped 100 meV into the conduction band (left) and valence band (right).

Usually, large band gap guarantees high specific heat of carriers, which is one of the reasons why the good TE materials are mostly semiconductors [48]. Moreover, we note that there is a fairly small dispersion in the valence band along the ΓA line, which makes the total EDOS increase very rapidly just below the VBM. Similar electron behavior can be also identified in the conduction band at about 0.71 eV above the CBM, which is resulted from the relatively flat band along the LA line, as shown in Fig. 4(a). These electron behaviors imply a large electron effective mass and thus high thermopower S. However, around the CBM there exists a fairly strong dispersion, which hints a high electron mobility, and consequently a high electrical conductivity σ if the carrier concentration is high enough. To further reveal the electron behavior around the CBM and VBM, we check the isoenergy (Fermi surface) of α-HgS for Fermi level E_F dipped a little into the conduction band and valence band. At 100 meV above the CBM, there is a spheroidlike isoenergy at the BZ center, as shown in Fig. 4(b), which implies a strong dispersion in all directions. At 100 meV below the VBM, there exists a plicated cylinderlike isoenergy along the ΓA line, which explains the quasi step function EDOS of α-HgS considering that strictly two-dimensional cylinder results in a step function EDOS. Similar character was also detected at 250 meV below the VBM in PbTe [49].

To calculate the electronic transport properties quantitatively, the electron Boltzmann theory and the rigid band approach with the $\mathbf{k}$ dependent electron relaxation time $\tau^{el}_{n\mathbf{k}}$ are used. In perfect crystalline samples, the electron scattering originates mainly from the EPI, thus the electron relaxation

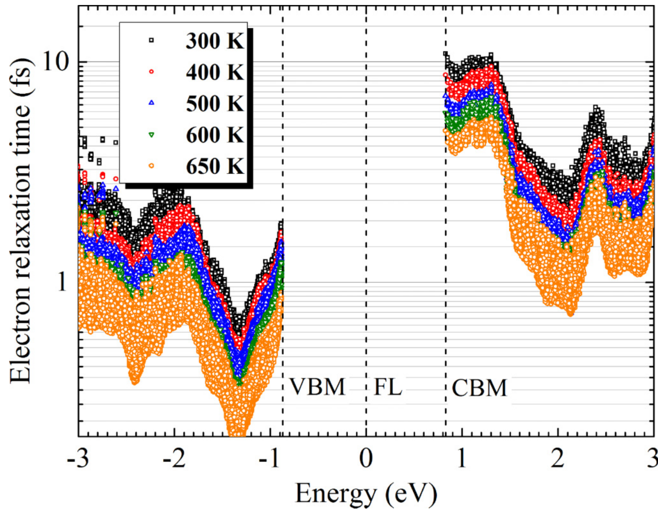

FIG. 5. Distribution of electron relaxation time in energy space at different temperatures. The energy range is the same as that in Fig. 4(a), and the three vertical dashed lines represent the sites of the valence band maximum (VBM), Fermi level (FL), and conduction band minimum (CBM), respectively.

time $\tau_{n\mathbf{k}}^{el}$ can be computed from the EPI matrix. According to Eqs. (5) and (6), electron relaxation time $\tau_{n\mathbf{k}}^{el}$ and EPI matrix are related by the electron linewidth $\Sigma_{n\mathbf{k}}''$, which is an indicator of the strength of the EPI. Our calculations show that the electron linewidths $\Sigma_{n\mathbf{k}}''$ of the conduction band are much smaller than those of the conduction band, as shown by the projections of electron linewidths on band structure in Fig. 4(a). This finding means that there is a weak EPI, large relaxation time $\tau_{n\mathbf{k}}^{el}$, and thus high electron mobility in the conduction band, being consistent with the band dispersion analysis. The distribution of electron relaxation time $\tau_{n\mathbf{k}}^{el}$ in energy space is shown in Fig. 5. Evidently, the electron relaxation time decreases as the increase of temperature, because a high temperature corresponds to a strong atomic vibration and thus strong electron scattering by phonon. At 300 K, the maximum relaxation time around the CMB is about 10.9 fs, which is much larger than the value of only 1.8 fs near the VBM, as shown in Fig. 5, and accords with the projections of electron linewidths on band structure.

Owing to the very high electron relaxation time of the conduction band and the lower lattice thermal conductivity along the a axis, the best TE performance is detected along the a axis of α-HgS with the n-type doping. The corresponding TE parameters calculated from Eqs. (2)–(4) are plotted in Fig. 6. Since the phase transition from α-HgS to β-HgS occurs at about 673 K [16], we only show the TE parameters below 650 K in Fig. 6. Due to the minus value of the thermopower S in α-HgS with the n-type doping, the $-S$ is plotted for convenience. As shown in Fig. 6(a), the $-S$ increases with temperature T at the same doping concentration n, and decreases with n at the same T, which is similar to the tendency observed in most of semiconducting TE materials. Remarkably, the values of the $-S$ are extraordinarily high, as is expected in the analyses of band structure. For instance, the $-S$ at $n \sim 1.6 \times 10^{19}$ cm^{-3} are in the range of 191 to 263 μVK^{-1} as T increases from 300 to 650 K. If the doping

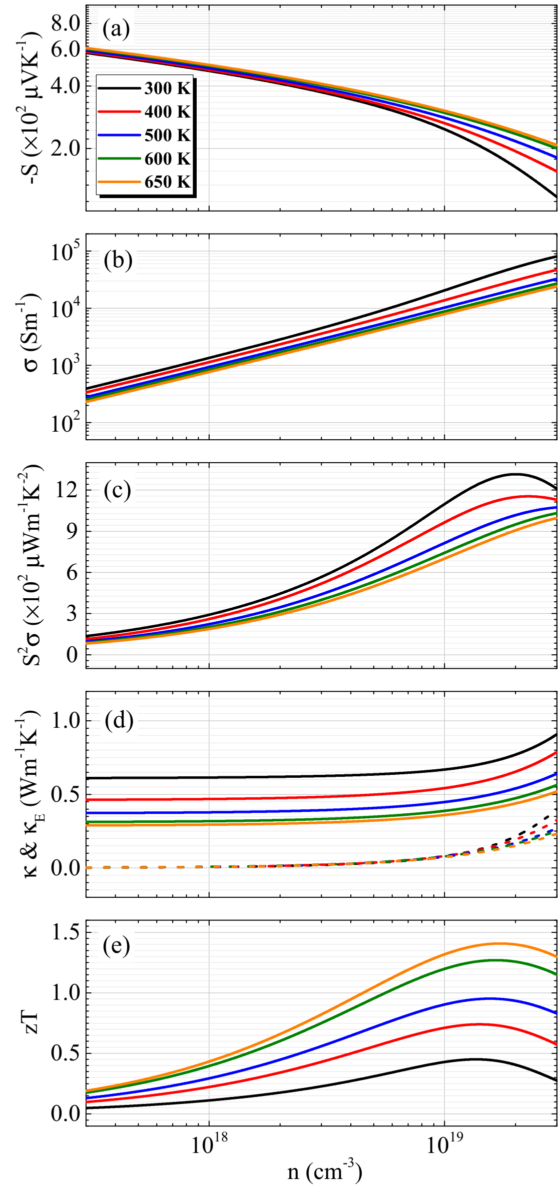

FIG. 6. Thermoelectric parameters along the a axis of the n-type doped α-HgS at 300 to 650 K: (a) Thermopower S. (b) Electrical conductivity σ. (c) Power factor $S^2\sigma$. (d) Total thermal conductivity κ (full lines) and electronic thermal conductivity κ_E (dash lines). (e) Figure of merit zT. In (b)–(e), the curves have the same color legend as that in (a).

concentration n lowers, $-S$ can be further enhanced, such as 247 μVK^{-1} at $n \sim 10^{19}$ cm^{-3} and $T = 300$ K. These values are very high compared with that of PbTe [3]. In view of that the typical thermopower for a high-zT material varies between 200 and 300 μVK^{-1}, these results hint a possible high zT in α-HgS.

The electrical conductivity σ is shown in Fig. 6(b), which indicates that σ decreases with T at the same n, and increases almost linearly with n at the same T, being consistent with the variation of electron relaxation time versus T and the relationship $\sigma \propto n$. The calculated power factor $S^2\sigma$ and the total thermal conductivity κ together with electronic thermal conductivity κ_E are shown in Figs. 6(c) and 6(d), respectively,

which exhibit a high $S^2\sigma$ and a quite low κ_E. For example, the $S^2\sigma$ at $n \sim 1.6 \times 10^{19}$ cm^{-3} are in the range of 1285 to 838 μWm^{-1} K^{-2} as T increases from 300 to 650 K, and the κ_E at the same n have the value of about 0.14 to 0.11 Wm^{-1} K^{-1} at $T = 300$ to 650 K, which takes up 19% to 28% of the total κ. As a result, in the n-type doped α-HgS a high figure of merit zT even exceeding 1.0 can be obtained along the a axis, as shown in Fig. 6(e). For instance, a high zT of 1.27 is reached at $n \sim 1.6 \times 10^{19}$ cm^{-3} and $T = 600$ K, and a zT of 0.74 (0.95) is achieved at 400 (500) K. Strikingly, a highest zT of 1.41 can be obtained at $n \sim 1.7 \times 10^{19}$ cm^{-3} if the temperature increases to 650 K. The concentration $n \sim 1.6 \times 10^{19}$ and 1.7×10^{19} cm^{-3} correspond to the electron doping of about 0.0027 e per unit cell, which can be accessible in experiments by atomic doping. In addition, for the n-type doped α-HgS there are also considerable TE performances along the c axis. For example, at $n \sim 5.2 \times 10^{19}$ cm^{-3}, the zT of 0.57 and 0.63 are realized along the c axis at 600 and 650 K, respectively (see S5 in Ref. [45]). These theoretical results indicate that α-HgS is a good candidate for TE applications.

Finally, we discuss the validity of our predictions for the electronic transport properties. Generally, the electronic transport and thermoelectric properties of a bulk material are calculated by the Boltzmann theory in constant relaxation time approximation (CRTA), where the electron relaxation time $\tau_{n\mathbf{k}}^{el}$ is taken as a turnable constant parameter τ_0^{el}, the conductivities σ and κ_E are determined within a factor of τ_0^{el}, and the thermopower S has no dependence on τ_0^{el} according to Eqs. (2)–(4). The parameter τ_0^{el} can be estimated from experimental data, simplified empirical model, or deformation potential model [7,8], etc. However, a more rigorous method is to calculate the electron relaxation time $\tau_{n\mathbf{k}}^{el}$ via the EPI [37], since the intrinsic electron scattering of a crystalline sample arises mainly from the EPI. In this method, besides the inclusion of the $\mathbf{k}$ dependence of the electron relaxation time in calculations of S, σ, and κ_E, there is no tunable empirical parameter in the whole computational process. To date the electronic transport and thermoelectric properties of a series of materials such as phosphorene [37], γ-graphyne [50], and monolayer MoS_2 [51,52], etc. have been investigated based on this parameter-free method, and the results of the monolayer MoS_2 have been confirmed to be well consistent with the experimental values [53–56]. Therefore, our electronic transport and thermoelectric properties of α-HgS obtained by this parameter-free method in the present work are deemed to be more predictable than those calculated by the empirical methods such as CRTA, although there is no corresponding available experimental result used for comparison at present.

IV. CONCLUSION

In summary, we have used the combination of first-principles calculations, Boltzmann transport equation, and electron-phonon interaction (EPI) to compute the thermal and electronic transport properties of α-HgS. The calculated lattice thermal conductivity κ_L is fairly low, which is resulted from the large weighted phase space and the quite low phonon group velocity. Based on EPI matrix, the $\mathbf{k}$ dependent electron relaxation time, thermopower S, electrical conductivity σ, and electronic thermal conductivity κ_E are calculated. Thanks to the presence of a flat band around the Fermi level and the large band gap, the calculated S is extraordinarily high. Compared with the valence band, the conduction band has a weaker EPI, smaller electron linewidths, larger electron relaxation time, and thus higher electrical conductivity σ. At the same time, the calculated electronic thermal conductivity κ_E of the n-type doped α-HgS takes up a much smaller portion of the total thermal conductivity κ. As a result, a high figure of merit zT even exceeding 1.4 is reached in α-HgS with the n-type doping. These results support that α-HgS is a good thermoelectric material. Considering that α-HgS can be refined from the mineral samples or grown from the elements by vapor phase techniques, experimental measurements are called for to verify our predictions.

ACKNOWLEDGMENTS

This research was supported by the National Natural Science Foundation of China under Grants No. 11704322, No. 11174171, and No. 11374175, the National Key Research and Development Program of China under Grants No. 2016YFB0700102 and No. 2016YFA0300902, the MOST Project of China under Grants No. 2012CB921403 and No. 2015CB921001, and the Natural Science Foundation of Shandong Province for Doctoral Program under Grant No. ZR2017BA017.

[1] K. Biswas, J. He, I. D. Blum, C.-I. Wu, T. P. Hogan, D. N. Seidman, V. P. Dravid, and M. G. Kanatzidis, Nature (London) **489**, 414 (2012).
[2] H. Wang, J.-H. Bahk, C. Kang, J. Hwang, K. Kim, J. Kim, P. Burke, J. E. Bowers, A. C. Gossard, A. Shakouri *et al.*, Proc. Natl. Acad. Sci. USA **111**, 10949 (2014).
[3] J. P. Heremans, V. Jovovic, E. S. Toberer, A. Saramat, K. Kurosaki, A. Charoenphakdee, S. Yamanaka, and G. J. Snyder, Science **321**, 554 (2008).
[4] Y. Pei, A. LaLonde, S. Iwanaga, and G. J. Snyder, Energy Environ. Sci. **4**, 2085 (2011).
[5] L. D. Hicks and M. S. Dresselhaus, Phys. Rev. B **47**, 12727 (1993).
[6] W. Liu, X. Tan, K. Yin, H. Liu, X. Tang, J. Shi, Q. Zhang, and C. Uher, Phys. Rev. Lett. **108**, 166601 (2012).
[7] Y. Zhao, Z. Dai, C. Zhang, C. Lian, S. Zeng, G. Li, S. Meng, and J. Ni, Phys. Rev. B **95**, 014307 (2017).
[8] Y. Zhao, Z. Dai, C. Lian, and S. Meng, RSC Adv. **7**, 25803 (2017).
[9] W. Li and N. Mingo, Phys. Rev. B **90**, 094302 (2014).
[10] L. Lindsay and D. S. Parker, Phys. Rev. B **92**, 144301 (2015).
[11] A. Roy, Phys. Rev. B **93**, 100101 (2016).
[12] W. Li and N. Mingo, Phys. Rev. B **91**, 144304 (2015).
[13] D. Bayerl and E. Kioupakis, Phys. Rev. B **91**, 165104 (2015).
[14] Q. Hao, D. Xu, N. Lu, and H. Zhao, Phys. Rev. B **93**, 205206 (2016).

[15] Rockwell International Corporation, US Patent Application No. 3914525 (1975).
[16] P. Ballirano, M. Botticelli, and A. Maras, Eur. J. Mineral. **25**, 957 (2013).
[17] E. Doni, L. Resca, S. Rodriguez, and W. M. Becker, Phys. Rev. B **20**, 1663 (1979).
[18] M. Pai, D. Buttrey, G. M. Joshi, and J. M. Honig, Phys. Rev. B **24**, 1087 (1981).
[19] S.-R. Sun, Y.-C. Li, J. Liu, Y.-H. Dong, and C.-X. Gao, Phys. Rev. B **73**, 113201 (2006).
[20] M. Cardona, R. K. Kremer, G. Siegle, A. Muñoz, A. H. Romero, and M. Schmidt, Phys. Rev. B **82**, 085210 (2010).
[21] R. Zallen, G. Lucovsky, W. Taylor, A. Pinczuk, and E. Burstein, Phys. Rev. B **1**, 4058 (1970).
[22] S. V. Gotoshia and L. V. Gotoshia, J. Phys. D: Appl. Phys. **41**, 115406 (2008).
[23] M. J. Peters, L. McNeil, and K. Dy, Solid State Commun. **97**, 1095 (1996).
[24] M. Abkowitz, G. Pfister, and R. Zallen, J. Appl. Phys. **43**, 2442 (1972).
[25] S.-H. Choe, K.-S. Yu, J.-E. Kim, H. Y. Park, and W.-T. Kim, J. Mater. Res. **6**, 2677 (1991).
[26] C. T. Simpson, W. Imaino, and W. M. Becker, Phys. Rev. B **22**, 911 (1980).
[27] C. Simpson, W. Imaino, W. Becker, and S. Faile, Solid State Commun. **28**, 39 (1978).
[28] G. Roberts, E. Lind, and E. Davis, J. Phys. Chem. Solids **30**, 833 (1969).
[29] G. Roberts and R. Zallen, J. Phys. C **4**, 1890 (1971).
[30] C. J. Vesely and D. W. Langer, Phys. Rev. B **4**, 451 (1971).
[31] W. Li, J. Carrete, N. A. Katcho, and N. Mingo, Comput. Phys. Commun. **185**, 1747 (2014).
[32] G. Kresse and J. Furthmüller, Phys. Rev. B **54**, 11169 (1996).
[33] G. Kresse and J. Furthmüller, Comput. Mater. Sci. **6**, 15 (1996).
[34] A. Togo, F. Oba, and I. Tanaka, Phys. Rev. B **78**, 134106 (2008).
[35] G. Kresse and D. Joubert, Phys. Rev. B **59**, 1758 (1999).
[36] J. P. Perdew, K. Burke, and M. Ernzerhof, Phys. Rev. Lett. **77**, 3865 (1996).
[37] B. Liao, J. Zhou, B. Qiu, M. S. Dresselhaus, and G. Chen, Phys. Rev. B **91**, 235419 (2015).
[38] S. Poncé, E. Margine, C. Verdi, and F. Giustino, Comput. Phys. Commun. **209**, 116 (2016).
[39] F. Giustino, M. L. Cohen, and S. G. Louie, Phys. Rev. B **76**, 165108 (2007).
[40] P. Giannozzi, S. Baroni, N. Bonini, M. Calandra, R. Car, C. Cavazzoni, D. Ceresoli, G. L. Chiarotti, M. Cococcioni, I. Dabo *et al.*, J. Phys.: Condens. Matter **21**, 395502 (2009).
[41] J. Noffsinger, F. Giustino, B. D. Malone, C.-H. Park, S. G. Louie, and M. L. Cohen, Comput. Phys. Commun. **181**, 2140 (2010).
[42] T. Schleid, P. Lauxmann, and C. Schneck, Z. Kristallogr., Supplement Issue **16**, 95 (1999).
[43] Z. Tian, J. Garg, K. Esfarjani, T. Shiga, J. Shiomi, and G. Chen, Phys. Rev. B **85**, 184303 (2012).
[44] J. He, M. Amsler, Y. Xia, S. S. Naghavi, V. I. Hegde, S. Hao, S. Goedecker, V. Ozoliņš, and C. Wolverton, Phys. Rev. Lett. **117**, 046602 (2016).
[45] See Supplemental Material at http://link.aps.org/supplemental/10.1103/PhysRevMaterials.1.065401 for the additional electronic, thermal, thermoelectric properties of α-HgS.
[46] W. Li and N. Mingo, Phys. Rev. B **89**, 184304 (2014).
[47] R. Zallen, in *II-VI Semiconducting Compounds*, edited by D. G. Thomas (Benjamin, New York, 1967), p. 877.
[48] G. J. Snyder and E. S. Toberer, Nat. Mater. **7**, 105 (2008).
[49] D. J. Singh, Phys. Rev. B **81**, 195217 (2010).
[50] P. Jiang, H. Liu, L. Cheng, D. Fan, J. Zhang, J. Wei, J. Liang, and J. Shi, Carbon **113**, 108 (2017).
[51] W. Li, Phys. Rev. B **92**, 075405 (2015).
[52] Y. Ge, W. Wan, W. Feng, D. Xiao, and Y. Yao, Phys. Rev. B **90**, 035414 (2014).
[53] X. Li, J. T. Mullen, Z. Jin, K. M. Borysenko, M. Buongiorno Nardelli, and K. W. Kim, Phys. Rev. B **87**, 115418 (2013).
[54] B. Radisavljevic, A. Radenovic, J. Brivio, i. V. Giacometti, and A. Kis, Nat. Nanotech. **6**, 147 (2011).
[55] M. S. Fuhrer and J. Hone, Nat. Nanotech. **8**, 146 (2013).
[56] B. Radisavljevic and A. Kis, Nat. Nanotech. **8**, 147 (2013).